Thermal gradient in polymeric particles during the cold spray process

Chrystelle A Bernard, H. Takana, G. Diguet, O. Lame, K. Ogawa, J. -Y. Cavaille

Thermal gradient in polymeric particles during the cold spray process

C.A. Bernard[a,b,c], H. Takana[d,e], G. Diguet[f], O. Lame[g], K. Ogawa[b,c], J.-Y. Cavaillé[b,e]

[a]Frontier Research Institute for Interdisciplinary Sciences, Tohoku University, Sendai, Japan
[b]ELyTMaX UMI3757, CNRS–Université de Lyon–Tohoku University, International Joint Unit, Tohoku University, Sendai, Japan
[c]Fracture and Reliability Research Institute, Tohoku University, Sendai, Japan
[d]Institute of Fluid Science, Tohoku University, Sendai, Japan
[e]Lyon Center, IFS - Tohoku University, Université de Lyon, INSAVALOR, Villeurbanne, 69621, France
[f]Micro System Integration Center, Micro/Nano-Machining Research and Education Center, Tohoku University, Sendai, Japan
[g]Materials Engineering and Science (MateIS), CNRS, INSA-Lyon, UMR5510, Université de Lyon, Villeurbanne, France

Abstract

Understanding the particle history during the cold spray process is primordial to better apprehend the particle's mechanical behavior during the impact. If the particle velocity can easily be measured using a high-speed camera, measuring the particle temperature remains a challenge. A solution is to perform numerical simulations of the process using computational fluid dynamics (CFD) simulations. However, most CFD simulation results only give an idea of the particle average temperature. Although it would be valid for metallic particles which exhibit a small temperature difference between the particle core and surface with high thermal stability, it is not the case for polymeric material, because of their low thermal conductivity.

In this paper, the thermal gradient of a polymer particle is investigated. While small particles exhibit a uniform temperature distribution, a large temperature gradient is observed for particle diameter larger than 30 µm. In addition, assuming that the particle is spherical without rotation during the flight, the particle exhibits melting at the front. Such a phenomenon can have considerable consequences on the particle behavior during the impact. Furthermore, the influence of the feeding rate on the particle temperature distribution is investigated. If the particles are well diluted inside the nozzle (low feeding rate) the difference in the average temperature of two successive particles is limited to 5 K.

Keywords

Thermal gradient, polymer, cold spray, sub-micron particles

Nomenclature

In the following, the subscript "p" refers to the particle while the subscript "g" refers to the gas. Parameters in **bold** are vectors. $\overline{\overline{\ }}$ refers to 3×3 tensors.

Dimensionless parameters

$\mathcal{B}_i$	Biot number
$\mathcal{N}_u$	Nusselt number
$\mathcal{P}_r$	Prandtl number
$\mathcal{R}_{e_p}$	Particle Reynolds number

CFD parameters

E	Total energy per unit of mass (J kg^{-1})

E_{melt}	Energy of melting of the crystalline lamellae (J)
E_T	Energy to increase the particle temperature (J)
$\mathbf{F}$	Force (N)
G_k	Generation of turbulence kinetic energy due to mean velocity gradients (W m^{-3})
G_b	Generation of turbulence kinetic energy due to buoyancy (W m^{-3})
k	Turbulent kinetic energy (J kg^{-1})
p	Gas pressure (Pa)
t	Time (s)
T	Absolute temperature (K)
$\boldsymbol{u}$	Velocity (m s^{-1})
Y_M	Contribution of the fluctuation dilatation in compressible turbulence to the overall dissipation rate (W m^{-3})
ε	Turbulent dissipation rate (m^2 s^{-3})

Heat transfer parameters

h	Convective heat transfer coefficient (W m^{-2} K^{-1})
H	Enthalpy (J kg^{-1})
$\boldsymbol{q}$	Heat flux by conduction (W m^{-2})
Q_s	Heat sources by conduction (W m^{-3})
Q_f	Heat sources by convection (W m^{-3})
$\bar{\bar{\tau}}$	Viscous stress tensor (Pa)

Material parameters

c_p	Heat capacity at constant pressure (J kg^{-1} K^{-1})
d_p	Particle diameter (m)
$H_{100\%}$	Enthalpy of fusion of a 100% crystalline material (J kg^{-1})
m_p	Particle mass (kg)
α_p	Thermal expansion coefficient (K^{-1})
ΔT	Temperature difference
Γ	Thermal conductivity (W m^{-1} K^{-1})
μ_g	Viscosity (Pa s)
μ_t	Turbulent viscosity (Pa s)
ρ	Density (kg m^{-3})
$\%\chi_c$	Crystallinity ratio

1. Introduction

Since its emergence in the 1980s, the cold spray process saw its popularity increasing. Initially discovered for metallic particles bonding on metallic substrates [1,2], the cold spray research found the opportunity to go beyond this scope. Thus, new research topics were revealed, focusing on coating functionalization such as metallization of ceramic, composite or polymer surfaces or polymer coatings to increase corrosion, wear resistance [3,4], and so on.

Since then, large insights into the particle history, adhesion, and deposition behavior have been made, especially regarding the impact of metallic particles on metallic substrates. In particular, Schmidt et al. [5] highlighted the existence and developed equations for the deposition windows for metallic

particles. These ones relate the particle velocity, temperature, diameter, and material properties to evaluate the particle critical velocity (starting velocity for which the adhesion is observed) and erosion velocity (starting velocity for which impacted particles erode the surface). The particle temperature and velocity are directly influenced by the working gas. Indeed, the cold spray process involves the acceleration of micro-sized particles through a de Laval nozzle using a pressurized heated gas. Thus, the gas flow has undoubtfully an influence on the particle behavior during its flight. While the inlet stagnation gas pressure will accelerate the particle, the inlet stagnation gas temperature will increase the particle temperature.

Even though the particle velocity can easily be measured experimentally using a fast camera and a laser [6], the same cannot be said for measuring the particle temperature. However, Nastic and Jodoin [7] successfully measured in-flight metallic particles temperatures during the cold spray process using a high-speed infrared camera. Close to the nozzle exit, the particle temperature appears higher, probably due to the influence of the nozzle's wall radiation on the particle (reflected temperature). However, far from the nozzle exit, a representative in-flight particle temperature can be obtained. This one appears to be in good agreement with the numerical predictions given by the computational fluid dynamics (CFD) simulations. Fiebig et al. [8] also used an high-speed infrared camera to measure the particle velocity and temperature of In718. They highlighted on the importance of the emissivity to obtain appropriate results for the particle temperature.

The gas dynamics plays an important role on the particle thermo-mechanical history during the cold spray process. Therefore, CFD simulations are essential to access the particle temperature. Three approaches can be identified [9]: (i) one-way coupling where the gas dynamics is computed independently and particles are considered as discrete phase, (ii) two-way coupling where gas/particle interaction is considered, and (iii) four-way coupling where gas/particle and particle/particle interactions are considered. Among these three approaches, the one-way coupling is conventionally used to simulate cold spray process under the assumption that the particles are well diluted in the flow field and therefore the influence of the particles on the gas dynamics can be neglected. Thus, particles are considered as material points, and no consideration of the particle volume is made. The particle history is determined following the particle equation of motion for the particle velocity, and the particle temperature is assumed to be uniform inside the particle at each instant. However, there is no reason for which the particle temperature should be homogeneous. To reach thermal equilibrium, time is needed comparatively to the material thermal properties (thermal conductivity and specific heat).

Katanoda [10] was one of the first to reveal the non-uniformity of the particle temperature during the cold spray process through the analysis of ceramic and metallic particle temperatures. By convection, the gas heats the particle surface, initiating a temperature difference with the particle core. Then, by conduction, the particle core is heated. For a 60 µm Al_2O_3 particle, Katanoda [10] evaluated the temperature difference inside the particle to be about 20~30 K before impact. This value is highly dependent on the particle diameter and material properties. Thus, the smaller the particle size, the smaller will be the temperature gradient, as the particle will thermalize more easily. Furthermore, depending on the material thermal properties, the particle thermal gradient can become negligible. Thus, Raoelison et al. [11] investigate the in-flight thermal gradient of several metallic particles. In particular, they showed that, during cold spray, the in-flight particle temperature difference is quite limited (<2 K) for a 50 µm Al particle due to the high thermal conductivity of these materials. Thus, in that case, the particle temperature, and therefore material properties, can be considered as homogeneous.

However, the same cannot be said for polymers. Polymers exhibit mechanical properties highly dependent on strain rate and temperature [12–15]. It is the reason why determining the thermo-mechanical history of the particle during its flight is primordial to further investigate the particle

impact behavior during cold spray. Recently, Bernard et al. [16] showed that during cold spray, the Biot number of polymer particles was larger than 1, revealing the presence of a thermal gradient within the particle, and therefore, a gradient of mechanical properties. Using a simple 2D axisymmetric model where only the evolution of the gas temperature was considered under constant flow velocity, they showed that the temperature difference could reach 25 K for a 60 µm polymer particle.

Bacha et al. [17] investigated the impact behavior of polyether ether ketone (PEEK) particles considering different thermal gradients for the particle. They showed that important shear stresses occur in the localized high-temperature regions. In addition, they showed that a hot particle surface is primordial for intra-particle adhesion. This can be explained by the possibility to induce co-crystallization at the interface of two particles [18] if their temperature is above the melting temperature.

Despite being widely used, the one-way coupling presents some issues that need to be addressed: (i) the flow dynamics is perturbated in the vicinity of the particles, and (ii) the particle/particle collision due to different velocities due to the large range of particle sizes, is omitted. This study is a direct continuation of our previous study [16] and the one of Raoelison et al. [11] (however, applied to polymers in this study). In addition to the gas temperature, in this study, we aim to analyze its coupling with the gas relative velocity. The physics coupling between the conduction/convection effect and the fluid flow dynamics are primordial to better access to the particle thermal history. For different particle diameters, the particle temperature map is investigated considering the gas temperature and the particle relative velocity experienced by the particle during its flight. Thus, the gas boundary conditions (pressure, temperature, relative velocity) are not constant but time dependent variables. Afterwards, the influence of the particle feeding rate will be investigated by introducing a second particle in the nozzle at a given distance from the first one. This analysis allows studying the interactions of one particle on its neighbors.

2. Modelling

Using a 2D axisymmetric model, our previous research [16] showed that the Biot number of ultra-high molecular weight polyethylene (UHMWPE) particles traveling inside a 240 mm long divergent nozzle experienced an important thermal gradient (Biot number larger than 1), and therefore, a gradient of mechanical properties. In this previous research, only the time dependence of the gas temperature was considered. In the present paper, the previous model has been improved by considering the gas relative velocity (= gas velocity - particle velocity) and the gas pressure as well. These input data are issued from previous calculations related to the fluid dynamics using ANSYS/FLUENT® 19.0 analysis [19].

The model complete description is available in [19], and only a summary of the model and equations used for simulating the fluid dynamics are presented here. The model includes both the cold spray nozzle, the substrate (at a standoff distance of 10 mm), and the powder feeder. Particles are injected on all the surface of the powder feeder and the Discrete Phase toolbox of FLUENT allows following their history inside the nozzle (trajectory, velocity, temperature).

2.1. Gas dynamics in the nozzle

The gas dynamics was investigated by computational fluid dynamics (CFD) simulations using ANSYS/Fluent 19.0. Details of the model and boundary conditions used are described in [19]. The gas velocity and temperature, and the particle velocity could be accessed assuming that (i) the gas flow is compressible and turbulent, (ii) the nozzle's wall and substrate are adiabatic, (iii) the gas is air, and (iv) the particles are assumed to be spherical. The Reynolds Averaging Navier Stokes (RANS) equations

coupled with the Realizable $k-\varepsilon$ model were used to describe the turbulent flow. Thus, the governing equations are:

- Continuity equation

$$\frac{\partial \rho_g}{\partial t} + \nabla \cdot \left(\rho_g \boldsymbol{u}_g\right) = 0 \tag{1}$$

- Momentum equation

$$\frac{\partial}{\partial t}\left(\rho_g \boldsymbol{u}_g\right) + \nabla \cdot \left(\rho_g \boldsymbol{u}_g \otimes \boldsymbol{u}_g\right) = -\nabla \mathrm{p_g} + \nabla \cdot \left(\left(\mu_\mathrm{g} + \mu_t\right)\left(\nabla \boldsymbol{u}_g + \nabla^\mathrm{T} \boldsymbol{u}_g - \frac{2}{3}\nabla \cdot \left(\boldsymbol{u}_\mathrm{g}\mathbb{I}\right)\right)\right) \tag{2}$$

- Energy equation

$$\frac{\partial}{\partial t}\left(\rho_g E_g\right) + \nabla \cdot \left(\boldsymbol{u}_g\left(\rho_g E_g + \mathrm{p_g}\right)\right) = \nabla \cdot \left(\Gamma_{eff} \nabla T_g + \bar{\bar{\tau}}_{eff} . \boldsymbol{u}_g\right) \tag{3}$$

- Transport equations

$$\begin{cases} \dfrac{\partial}{\partial t}\left(\rho_g k\right) + \nabla \cdot \left(\rho_g k \boldsymbol{u}_g\right) &= \nabla \cdot \left(\left(\mu_g + \dfrac{\mu_t}{\mathcal{P}_{r_k}}\right)\nabla k\right) + G_k + G_b - \rho_g \varepsilon - Y_M \\ \dfrac{\partial}{\partial t}\left(\rho_g \varepsilon\right) + \nabla \cdot \left(\rho_g \varepsilon \boldsymbol{u}_g\right) &= \nabla \cdot \left(\left(\mu_g + \dfrac{\mu_t}{\mathcal{P}_{r_\varepsilon}}\right)\nabla \varepsilon\right) + 1.44\dfrac{\varepsilon}{k}\left(G_k + C_\varepsilon G_b\right) - 1.92\rho_g \dfrac{\varepsilon^2}{k} \end{cases} \tag{4}$$

where ρ_g is the gas density, $\boldsymbol{u}_g$ is the gas velocity, $\mathrm{p_g}$ is the gas pressure, $\mu_\mathrm{g}$and μ_t are laminar and turbulent gas viscosities, $\mathbb{I}$ is the identity tensor, $\mathrm{E_g}$ is the total energy, Γ_{eff} is the effective thermal conductivity and $\bar{\bar{\tau}}_{eff}$ is the effective stress tensor. k is the turbulence kinetic energy, and ε is the turbulence dissipation rate. G_k and G_b are related to the generation of turbulence kinetic energy, and Y_M represents the contribution of the fluctuating dilatation in compressible turbulence to the overall dissipation rate. $\mathcal{P}_{r_k} = 1$ and $\mathcal{P}_{r_\varepsilon} = 1.3$ are Prandtl number related to k and ε, respectively [20]. C_ε is a constant, and ∂t and ∇ are time and spatial derivative. Symbols in **bold** represents vector, while $\bar{\bar{}}$ represents tensor.

Particles, considered as discrete phase, are injected on the particle inlet surface. Considering the particle as spherical, the equation of motion on the particle is given by:

$$m_p \frac{d\boldsymbol{u}_p}{dt} = \mathbf{F} \tag{5}$$

where m_p, $\boldsymbol{u}_p$ are the particle mass and velocity, and $\mathbf{F}$ represents the overall forces acting on the particle including the gravity, drag force, Saffman lift force, and the thermophoretic force.

Based on these calculations, the gas pressure, the gas temperature, and the particle relative velocity defined as the difference between the gas and the particles, is obtained as reported in Figure 1 for a 60 µm diameter particle. A large range of particle sizes has been investigated. Details are provided in Supplementary file 1.

Assuming that the particles are spherical is quite a strong hypothesis for polymer particles as, as shown by the micrographs of Ravi et al. [21], the polymer particle geometry is relatively coarse. Therefore,

during the flight, the particles are more likely to align in the privileged direction to minimize the drag force. For this reason, no particle rotation was considered in this work. However, near the boundary layer (nozzle wall), the particle velocity can momentarily be higher than the gas velocity. This was considered through the change of sign in the gas relative velocity, as shown in Figure 1.

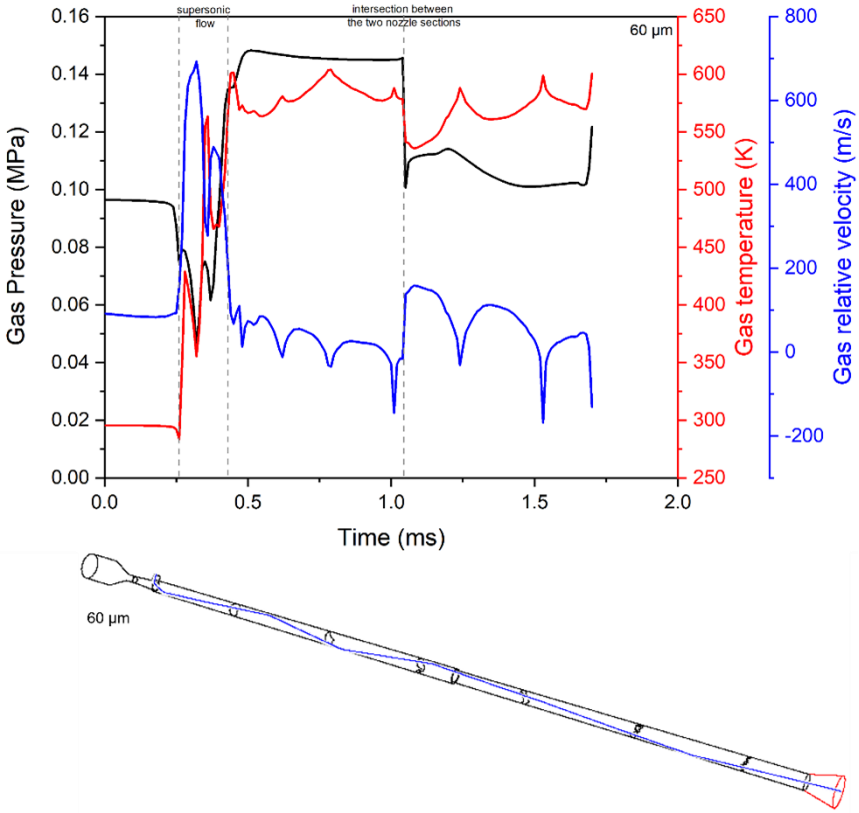

Figure 1: Time evolution of the gas temperature, pressure, and relative velocity around a 60 µm particle and related particle trajectory. These data obtained from CFD simulations will be given as boundary conditions for the particle heating simulation during its flight. The decrease in the particle velocity in the nozzle are related to the particle rebound on the nozzle wall. In the boundary layer, the fluid velocity is lower than the particle velocity which explains this phenomenon.

2.2. Evolution of the particle temperature: FEM approach

Based on the previous calculations, a numerical approach based on the finite element method (FEM) is designed. The model uses a multiphysics approach combining fluid mechanics and heat transfer (conduction and convection) to evaluate the evolution of the particle temperature during its flight. The model geometry and boundary conditions are described in Figure 2. A particle of diameter d_p is isolated in a fluid (gas) domain of dimension $\max(20d_p, 4\text{ mm}) \times 40d_p$; 4 mm being the diameter of the nozzle at the particle entrance.

COMSOL Multiphysics 6.0 is used to perform the simulations with "Laminar Flow" and "Heat Transfer in Solids and Fluids" modules. Additionally, relationships between the fluid dynamics and the convection/conduction exist to better account for the interface between the particle and the gas.

The conduction effect in the solid is governed by:

$$\rho_p c_{p,p} \frac{\partial T_p}{\partial t} + \nabla \cdot \boldsymbol{q} = Q_s \tag{6}$$

where $\boldsymbol{q}$ is the heat flux by conduction equals to $-\Gamma_{\mathrm{p}}\nabla T$ and Γ_p is the particle conductivity, $c_p$is the thermal conductivity, T is the particle absolute temperature, and Q_s regroups different heat sources in the solid.

The convection effect in the fluid is governed by:

$$\rho_g c_{p,g}\left(\frac{\partial T_g}{\partial t}+\boldsymbol{u}_g\cdot\nabla T_g\right)+\nabla\cdot\boldsymbol{q}=\alpha_g T_g\left(\frac{\partial \mathrm{p_g}}{\partial t}+\boldsymbol{u}_g\cdot\nabla \mathrm{p_g}\right)+\bar{\bar{\tau}}\colon\nabla\boldsymbol{u}_g+Q_f \tag{7}$$

where $\bar{\bar{\tau}}$ is the viscous stress tensor, α_p is the thermal expansion coefficient, and Q_f regroups different heat sources in the fluid.

Two types of interfaces are defined at the particle/gas boundaries, depending on whether the front or the back of the particle (part of the particle surface hitting first the substrate) is considered:

$$-\boldsymbol{n}\cdot\boldsymbol{q}=\begin{cases}\rho\Delta H\boldsymbol{u}_g\cdot\boldsymbol{n} & \text{if front of the particle}\\ 0 & \text{if behind the particle}\end{cases} \tag{8}$$

where the enthalpy is defined by

$$\Delta H=\int_{T_{ustr}}^{T}c_p dT_g \tag{9}$$

where T_{ustr} is the upstream temperature given by the CFD calculations (see Figure 1).

To model the fluid dynamics in the Multiphysics model, laminar flow is used, unlike the $k-\varepsilon$ turbulence model used in the CFD model. The reasons of this choice are the following: 1) the gas temperature, velocity, pressure are given by the CFD calculation using the $k-\varepsilon$ turbulence model described above; 2) the supersonic flow is a localized phenomenon, so it is considered not to disturb much the flow field around the particle. Therefore, the governing equations of the flow field are reduced to the continuity, momentum, and energy equations defined in equations (1)-(3). At the inlet, the gas flow field is described by the time evolution of its temperature and relative velocity. At the outlet, the time evolution of the gas pressure is introduced. At the particle/gas interface, the gas velocity is assumed to be null. The lateral walls of the gas domain are defined by a slip condition for the gas flow on the wall surface. The use of these boundary conditions is here to represent that only a part of the fluid domain is modeled, if we assume that the overall fluid domain covers all the space included inside the cold-spray nozzle. Thus, Dirichlet conditions are used on the lateral wall of the gas domain.

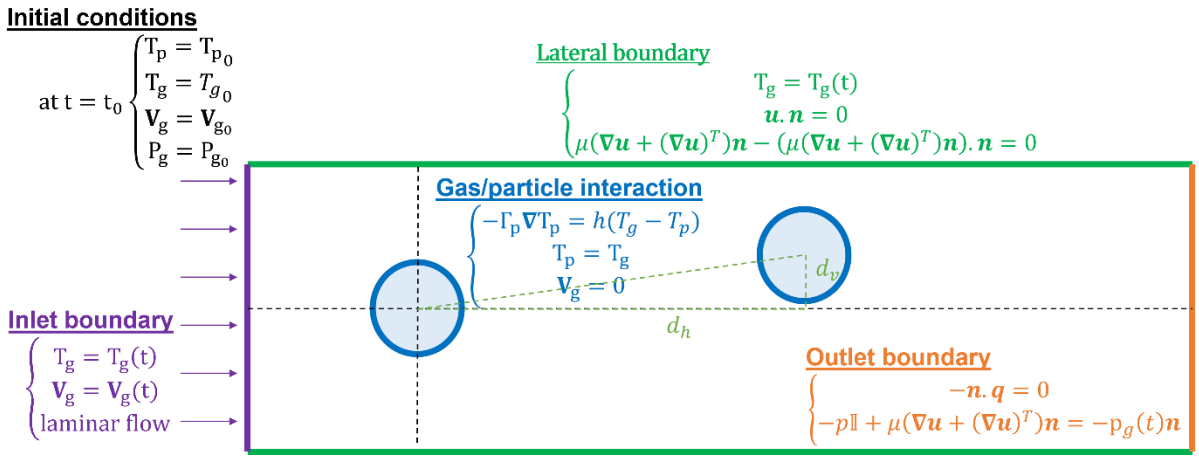

Figure 2: Schematic of the finite element model with boundary conditions to evaluate the particle temperature during its flight. This model is based on the model used by Raoelison [11]. The differences between the two models lies in the definition of the boundary conditions: gas temperature, pressure, and relative velocity, which are, in this work, time dependent.

The model is discretized with around 53,000 3D linear tetrahedral elements distributed in 3 domains corresponding to (i) the particle with a mesh size of $d_p/20$, (ii) a first fluid domain with a fine mesh of $d_p/3$ to capture the evolution of the flow field close and behind the particle, and (iii) a second fluid domain with a maximum mesh size of 0.13 mm far from the particle.

Later, a second particle will be introduced in the model (see Figure 3). This one has the same size as the first particle. Therefore, we can assume the same initial conditions for gas temperature, pressure, and relative velocity. The second particle is located at coordinates (d_h, d_v) relatively to the first particle, with d_h ranging from 3d to 31d, and d_v ranging from 0 to 2.4d, with d, the particle diameter, set at 60 µm. This analysis allows investigating the influence of the powder feeding rate on the particle temperature. Usually, during the cold spray process, the particle flux is assumed to be diluted in the gas flux. This study is here to check the extent of this assumption.

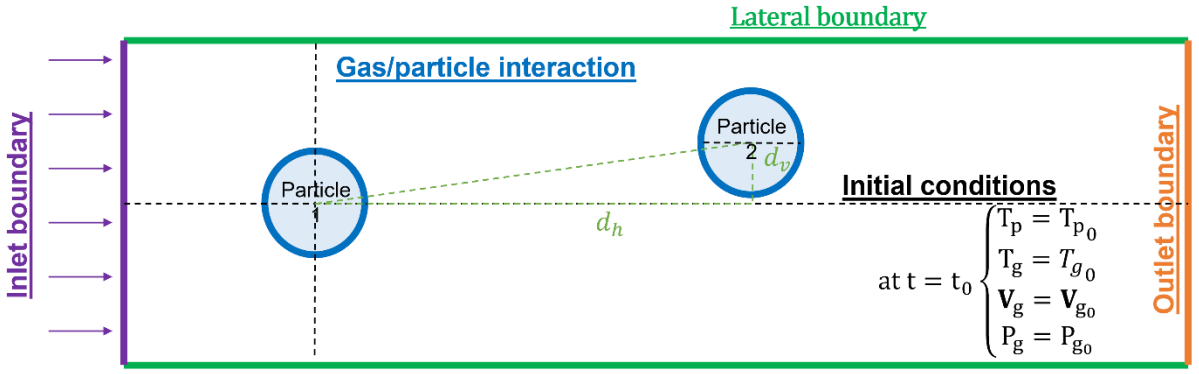

Figure 3: Schematic of the finite element model used to evaluate the particle temperature and its influence on the neighboring particles. The same boundary conditions as presented in Figure 2 are used.

2.3. Powder material and properties

This study investigates the temperature evolution of ultra-high molecular weight polyethylene (UHMWPE), previously studied for cold spray by Ravi et al. [21,22]. Details of the material and thermal properties are presented in Table 1.

Table 1: Material and thermal properties of UHMWPE particles.

Particle Material	**UHMWPE**

Diameter, d_p	$10{\sim}250$ µm
Density, ρ_p	940 kg m^{-3}
(Solid) Specific heat at 298 K, $c_p^s(298\ \mathrm{K})$	1807 J kg^{-1} K^{-1}
(Liquid) Specific heat at 298 K, $c_p^l(298\ \mathrm{K})$	2167 J kg^{-1} K^{-1}
Thermal conductivity at the melting temperature, Γ_m	0.41 W m^{-1} K^{-1}
Melting temperature, T_m	413 K

It is well-known that polymer properties exhibit a strong temperature dependence especially near its transition temperatures. This is true for its mechanical properties (elastic modulus, yield strength, etc.) but also thermal properties such as specific heat and thermal conductivity.

While amorphous polymers' behavior is governed by the glass transition temperature, the transition temperature for semi-crystalline polymers is more related to the melting temperature, at least for the evolution of the thermal properties. Bicerano [23], van Krevelen and te Nijenhuis [24] established analytical models for the specific heat and thermal conductivity of amorphous polymers based on the discontinuity of these properties at the glass transition temperature (C_1 function). As a similar phenomenon is observed near the melting temperature of semi-crystalline, the same equations can be used while adjusting the transition temperature. Therefore, as a function of the temperature, the specific heat is defined as:

$$c_p(T_p) = \begin{cases} c_p^s(298\ \mathrm{K}) * \left[0.106 + 3 \times 10^{-3} T_p\right] & \text{if} \quad T_p < T_m \\ c_p^l(298\ \mathrm{K}) * \left[0.61 + 1.3 \times 10^{-3} T_p\right] & \text{if} \quad T_p > T_m \end{cases} \tag{10}$$

and the thermal conductivity as:

$$\Gamma_{\mathrm{p}}(T_p) = \begin{cases} \Gamma_m \left(\dfrac{T_p}{T_m}\right)^{0.22} & \text{if} \quad T_p < T_m \\ \Gamma_m \left(1.2 - 0.2\dfrac{T_p}{T_m}\right) & \text{if} \quad T_p > T_m \end{cases} \tag{11}$$

where T_p is the absolute temperature of the particle. It should be noted that during its flight, the particle temperature should not exceed the polymer melting temperature at the risk of clogging the nozzle.

In addition, an exponential increase in the specific heat is observed in the vicinity of the melting temperature due to the melting of the crystalline lamellae [24]. This aspect was considered via the heat flow curve of UHMWPE given by Ravi et al. [21]. The evolution of the specific heat and thermal conductivity as a function of the temperature is plotted in Figure 4.

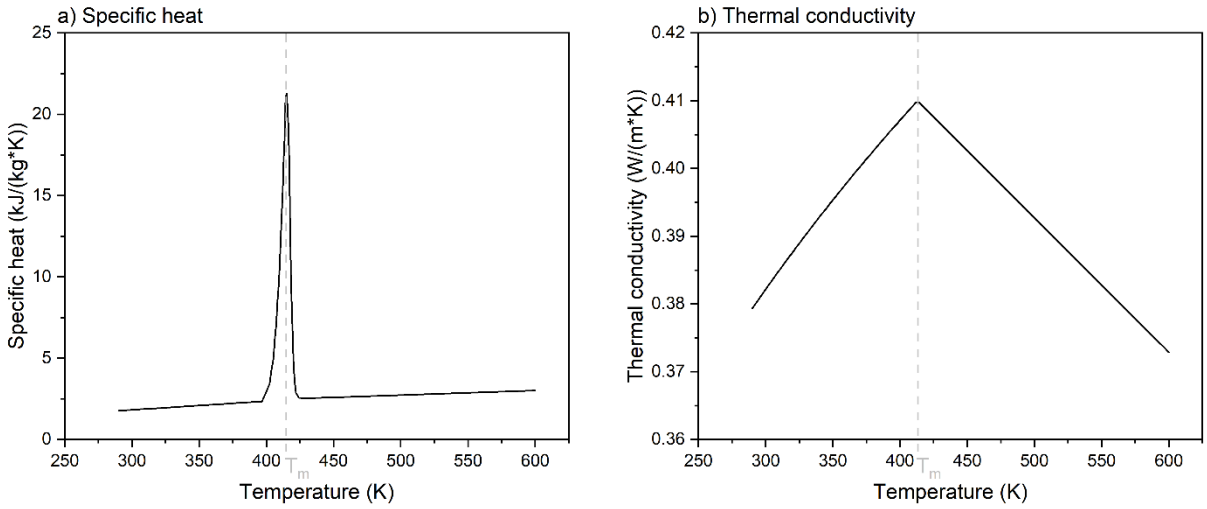

Figure 4: Evolution of the a) specific heat and b) thermal conductivity of UHMWPE as a function of the temperature.

2.4. Evolution of the particle temperature: Analytical approach

An analytical approach to evaluate the particle temperature is also considered. Unlike the analytical approaches adopted by Katanoda [10] or Raoelison et al. [11], who consider the particle equation of motion using the theoretical solution for the fluid flow (isentropic model), in this study, the gas temperature, relative velocity, and pressure are given by the CFD simulations. Several authors [25–27] highlighted the overestimation of the particle velocity of the isentropic model by 5 to 10% as it does not consider the gas flow and shock wave. This has undoubtfully an influence on the gas temperature and particle resident time inside the nozzle, therefore on the particle temperature. Thus, the accuracy given by Fluent is higher. In addition, comparing the analytical study by Ravi et al. [28] with the computational simulation by Bernard et al. [16] on the same material/nozzle, large overestimation of the gas velocity and particle temperature, and also large underestimation of particle velocity and gas temperature is observed. As the purpose of this work is to look closely at the particle temperature distribution, results for the gas temperature, pressure, and relative velocity are preferred over the results of the isentropic model.

From an analytical viewpoint, considering axisymmetric heat conduction, the evolution of the particle temperature is given by the following equation of heat conduction:

$$\rho_p c_p \frac{\partial T_p(r,t)}{\partial t} = \frac{1}{r^2}\left(\frac{\partial}{\partial r}\left(r^2 \Gamma_p \frac{\partial T_p(r,t)}{\partial r}\right)\right) \quad \text{with} \quad r \in \left[0, \frac{d_p}{2}\right] \tag{12}$$

with the following boundary conditions:

$$\begin{cases} T_p(r,0) & = & T_0 \\ -\Gamma_{\mathrm{p}} \left.\dfrac{\partial T_p(r,t)}{\partial r}\right|_{r=\frac{d_p}{2}} & = & h\left(T_g - T_p\left(\dfrac{d_p}{2}, t\right)\right) \\ T_p(r,\infty) & = & T_g \end{cases} \tag{13}$$

where h is the heat transfer coefficient. In addition, when $t \to \infty$, the particle is thermalized, and therefore, at the gas temperature. Details of the calculations is given in Supplementary file 2, where

$$T_p(r,t) = 2(T_0 - T_g)\sum_{n=1}^{\infty} \exp\left(-\frac{4\alpha_p \Lambda_n^2 t}{{d_p}^2}\right)\left[\frac{3\mathcal{B}_i \cos(\Lambda_n)}{1 - 3\mathcal{B}_i - \cos^2(\Lambda_n)}\right] \frac{\sin\left(2\Lambda_n \frac{r}{d_p}\right)}{2\Lambda_n \frac{r}{d_p}} + T_g \quad (14)$$

in agreement with the formulation of the particle temperature given by Raoelison et al. [11] with minor corrections. As Raoelison et al. [11] already demonstrated the accuracy of this formulation, it will not be discussed here. In eq. (14), $\alpha_p = \frac{\Gamma_p}{\rho_p c_p}$ is the thermal diffusivity, Λ_n are eigenvalues, solution of the transcendental equation

$$\frac{\Lambda}{\tan(\Lambda)} = 1 - 3\mathcal{B}_i \quad (15)$$

and $\mathcal{B}_i$ is the Biot number defined for a sphere by:

$$\mathcal{B}_i = \frac{h d_p}{6\Gamma_p}. \quad (16)$$

The Biot number is a dimensionless number in heat transfer. Thus, if the Biot number is below 0.1, the temperature can be assumed homogenous within the particle. On the contrary, when the Biot is above 0.1, such an assumption is not valid anymore. A thermal gradient exists within the particle and generally leads to a gradient of thermal properties. In the case of polymer particles, several authors [16,17,29,30] highlighted the importance of this thermal gradient for a better understanding of polymer coating by the cold spray process.

To solve eq. (15), it is necessary to determine the value of $\mathcal{B}_i$ for the different particle sizes. However, as mentioned by Nastic and Jodoin [7], it is not an easy task to determine the convective heat transfer coefficient during the cold spray process. One of the solutions is to calculate h through the calculation of the Nusselt number $\mathcal{N}_u$, dimensionless number characterizing the heat transfer in a fluid:

$$\mathcal{N}_u = \frac{h d_p}{\Gamma_g}. \quad (17)$$

For a forced flow around a sphere, Ranz and Marshall [31] express the Nusselt number under the simplified expression:

$$\mathcal{N}_u = 2.0 + 0.6{\mathcal{P}_r}^{0.33}{\mathcal{R}_{ep}}^{0.5} \quad (18)$$

where $\mathcal{P}_r$ is the Prandtl number and $\mathcal{R}_{ep}$ is the particle Reynolds number defined as:

$$\begin{cases} \mathcal{P}_r &= \dfrac{c_{p,g}\mu_g}{\Gamma_g} \\ \mathcal{R}_{ep} &= \dfrac{\rho_g |\mathbf{u}_g - \mathbf{u}_p| d_p}{\mu_g} \end{cases} \quad (19)$$

In the context of this study, the working gas is air. The air pressure ρ_g is given from the equation of state as an ideal gas:

$$\rho_g = \frac{\mathrm{p_g}}{R_{specific} T_g} \quad (20)$$

where $R_{specific} = 287\ \mathrm{J\,kg^{-1}\,K^{-1}}$ is the specific gas constant of air. For thermal conductivity Γ_g, specific heat capacity $c_{p,g}$ and viscosity μ_g, their pressure dependence in the range of $0.1{\sim}0.5$ MPa is relatively small for all temperatures. Thus, the temperature dependence of the air specific heat capacity is given by [32]:

$$c_{p,g}(T_g) = 1030 - 365\frac{T_g}{1000} + 850\left(\frac{T_g}{1000}\right)^2 - 390\left(\frac{T_g}{1000}\right)^3. \quad (21)$$

The temperature dependence of the air viscosity is given by Sutherland equation [33]

$$\mu_g(T) = \mu_{ref}\frac{(T_{ref} + C)}{T + C}\left(\frac{T_g}{T_{ref}}\right)^{3/2} \quad (22)$$

where $T_{ref} = 293$ K, $C = 117$ K, and $\mu_{ref} = 18.2 \times 10^{-6}$ Pa s.
The temperature dependence of the thermal conductivity is given by [34]:

$$\Gamma_g(T) = \frac{a\sqrt{T_g}}{1 + b \times \frac{10^{-c/T_g}}{T_g}} \quad (23)$$

where a, b, c are constant equal to 2.6462×10^{-3} W m^{-1} K$^{-3/2}$, 245.4 K, and 12 K, respectively.

It should be noted that the equation for the particle temperature (eq. (14)) was obtained considering a constant gas temperature over the entire domain, as well as constant relative gas velocity, and air/particle properties. However, as observed in eqs. (10)-(11) and (20)-(23), all the properties are given as a function of temperature.

3. Results and Discussion

3.1. Particle melting

While travelling inside the nozzle, the polymer particles are not exempt to melt depending on their size, thermal properties, microstructure, but also on the process parameters (gas temperature, resident time, etc.). Determining if a particle is susceptible to melting is of prime importance to select the appropriate particle size in order to avoid nozzle clocking.

The energy needed for melting one particle is given by:

$$E_{melt} = m_p \times (H_{100\%} \times \%\chi_c + c_p \Delta T) \quad (24)$$

where E_{melt} is the melting energy, $m_p = \rho_p * \frac{4}{3}\pi r_p^3$ is the particle mass and r_p the particle radius. $H_{100\%}$ is the enthalpy of fusion of a 100% crystalline material (equals to 290 J g^{-1} for an UHMWPE), $\%\chi_c$ is the crystalline ratio of the powder (equals to 56% [21]), ΔT is the temperature difference between the initial and final temperature of the particle, and c_p the average specific heat equals to 2220 J kg^{-1} K^{-1} [21]. This value of specific heat corresponds to an averaged value over the temperature range.

However, during the CFD calculation, particle melting was not considered, and only the particle temperature increase was calculated. Thus, in absence of melting, the energy equation is reduced to

$$E_T = m_p c_p \Delta T \quad (25)$$

where E_T represents the amount of energy to increase the temperature of ΔT.

For a couple of particle diameters, the energy needed for melting the particle and the energy to increase the particle temperature are presented in Table 2. The temperature difference is obtained

from our previous work [19], where the average particle temperature was calculated using ANSYS/Fluent for different particle diameters. The energy analysis (eqs. (24) and (25)) shows that 10 µm particles are clearly melting. Regarding 20 and 30 µm particles, it is interesting to note that despite presenting an average temperature higher than the melting temperature, the particles are not considered melted. Thus, for these particle sizes, it appears that, during the flight, the particles are not entirely melting. Only the particle's surface is melting, and the core remains below the melting temperature. However, regarding the energy calculated, it should be observed that the 20 µm UHMWPE particles are very close to melting completely (~10 K). Based on the results provided in Table 2, additional analysis has been performed to determine the particle size threshold value for which complete melting of the particle occurs. A linear interpolation of the energies between 10 and 20 µm shows that particles lower than 17.5 µm are susceptible to melting entirely and, therefore, should be discarded from the feedstock. Of course, this analysis to a first approximation where the specific heat is averaged to a constant value (2220 J/(kg/K)).

Table 2: Energy of melting and energy to increase the particle temperature for different particle diameters. ΔT is obtained from our previous research [19] where $T_0 = 300\ K$. An average cp value of 2220 J/(kg K) has been taken for this analysis.

Diameter (µm)	**10**	**20**	**30**	**60**	**100**	**150**	**200**	**250**
$\boldsymbol{\Delta T = \langle T \rangle - T_0}$	243	175	115	56	36	26	19	15
Energy needed to melt the particle, E_{melt} (µJ)	0.20	1.63	5.5	43.9	203	686	1630	3180
Energy needed to increase the particle temperature without considering melting, E_T (µJ)	0.26	1.53	3.39	13.2	39.3	95.9	166.1	256.1
Melting if $E_T > E_{melt}$	**TRUE**	FALSE	FALSE	FALSE	FALSE	FALSE	FALSE	FALSE

3.2. Non-uniformity of the polymer particle temperature during the cold spray process

In the description of the analytical model, the Biot number intervenes as part of the solution of the transcendental equation (15). The Biot number is a function of the heat transfer coefficient, particle diameter, thermal properties of the particles and gas, and the relative gas velocity (eqs. (16)-(19)). While material properties are temperature dependent, the relative gas velocity is time dependent (as the gas temperature experienced by the particle in the nozzle). Thus, for each particle diameter and step time, a value of the Biot number has been calculated. Average of all the Biot number over the overall particle flight time has been plotted in Figure 5.

Assuming the particle is spherical, the threshold for the non-uniformity of the particle temperature (Biot number = 0.1) is close to 30 µm diameter for a UHMWPE polymer particle traveling in a 240 mm long divergent nozzle. For a Biot number smaller than 0.1, the particle temperature is considered homogeneous, while above this value, the assumption of homogeneous temperature does not stand anymore. In their experiments, Ravi et al. [21] sieved the UHMWPE powder and sprayed only the powder with a diameter of 45-63 µm. For this diameter range, it is obvious, from the calculation of the Biot number that the particle temperature is not homogenous anymore.

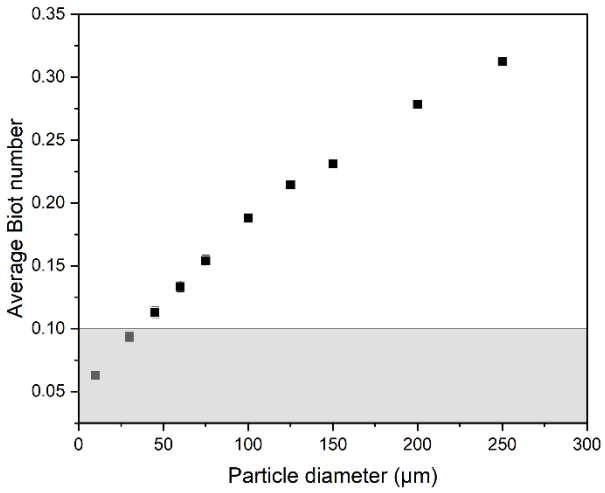

Figure 5: Evolution of the average Biot number as a function of the particle diameter.

3.3. Particle thermal gradient

In Figure 6a, the evolution of the particle temperature difference (obtained at the end of the particle flight time, just before its impact on the substrate) is plotted as a function of the particle diameter. The particle temperature difference ΔT is defined as the difference between the maximum T_{max} and the minimum temperature T_{min} calculated inside the particle at given time:

$$\Delta T(t) = T_{max}(t) - T_{min}(t) \tag{26}$$

The analytical model is compared with the results given from the CFD & heat transfer model. Even though discrepancy is observed between the two models in terms of the particle temperature difference, the average particle temperature is very close between the three models (analytical model, FEM using CFD (our former study [19] where the particle was assumed to be a discrete object), and FEM for CFD coupled heat transfer analysis,(this study where the volume and temperature distribution inside the particle are considered)) (see Figure 6b). A plausible explanation for the discrepancy between these three models comes from the differences in the analysis method. Thus, in the CFD model, the particle is considered as a material point with constant particle thermal properties. Assuming no particle rotation during the cold spray process, the particle heating is done unidirectionally, as shown in Figure 7. On the contrary, the analytical model considers radial heating of the particle, with temperature dependent material properties calculated at each time step (therefore, as a function of the gas temperature). However, the resolution of equations (14) and (15) assumes constant Biot number and gas temperature averaged over all the particle flight time.

The model combining CFD and heat transfer models takes advantage of the analytical model and CFD model to evaluate the temperature within the particle during its flight, and therefore reproduces the particle heating during the cold spray process. Thus, it considers unidirectional flow velocity combined with time dependent gas temperature, pressure and relative velocity (such as experienced by the particle during its flight), and temperature dependent particle and gas properties. Thus, it allows obtaining more accurate information of the particle temperature during its flight and before impact on the substrate.

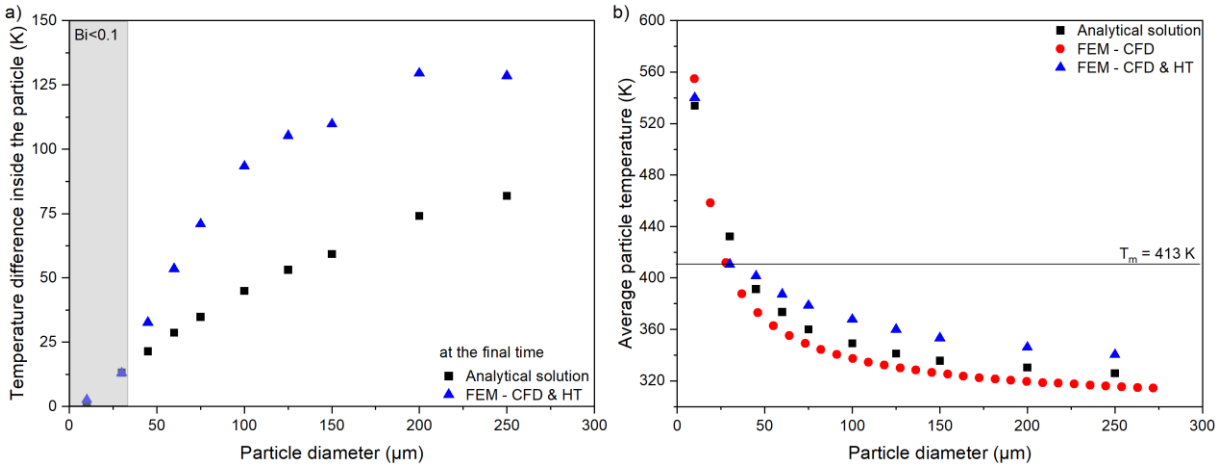

Figure 6: a) Evolution of the particle temperature difference as a function of the particle diameter. b) Comparison of the average particle temperature between the analytical model and FEM models considering only the fluid dynamics (Fluent) and the coupling fluid dynamics and heat transfer (COMSOL). The calculation labeled "FEM-CFD" and "Analytical solution" considered a constant average specific heat of 2220 j kg^{-1} K^{-1}, in agreement with [21].

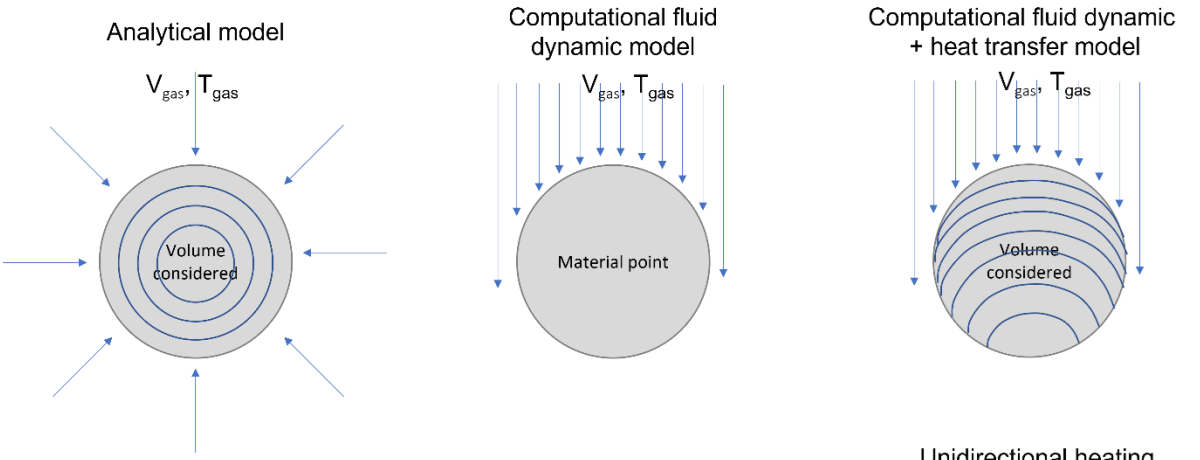

Figure 7: Schematic of the particle temperature calculation for the different models.

In Figure 8, the evolution of the particle temperature along the symmetry axis of the model (as defined in Figure 2) is plotted for the different particle diameters investigated at the final time (before the particle impacts on the substrate). As expected, from Figure 6b, the temperature of 10 and 30 µm diameter particles are above the melting temperature of the UHMWPE. This suggests that these particle sizes are more likely susceptible to clog the nozzle during the spray. For larger particles, only the particle front exhibits a temperature higher than the particle melting temperature. Thus, this localized phenomenon will not induce clogging of the nozzle. It is interesting to note that the particle's bottom is also heated by the gas flux, thanks to the presence of vortices during the particles' flight. Finally, the incoming gas and the vortices heat the particle surface, which by conduction contributes to heat the particle core. However, for large particles, the temperature at the particle's core remains

close to the particle initial temperature. Thus, the conduction effects are minimum in front of the particle volume and resident time inside the nozzle.

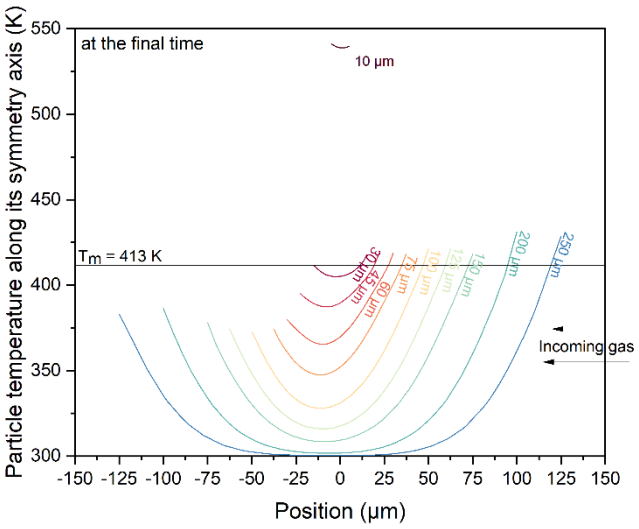

Figure 8: Particle temperature distribution along the symmetry axis (as defined in Figure 2) before the particle impact on the substrate.

Figure 9 shows the evolution of the largest temperature difference within the particle as a function of the particle resident time and particle velocity for the different investigated particle diameters. Depending on its diameter, the particle velocity, and therefore, resident time, is different. Thus, the increase in the resident time is linked to an increase in the particle diameter, and a decrease in the particle velocity. As the particles become bigger, the heating by thermal conduction is reduced due to the increase of the particle volume, which leads to an important temperature difference inside the particle. Exception is made for the 10 µm diameter particle which exhibits a lower velocity than the 30 µm diameter due to the presence of the bow-shock in front of the substrate.

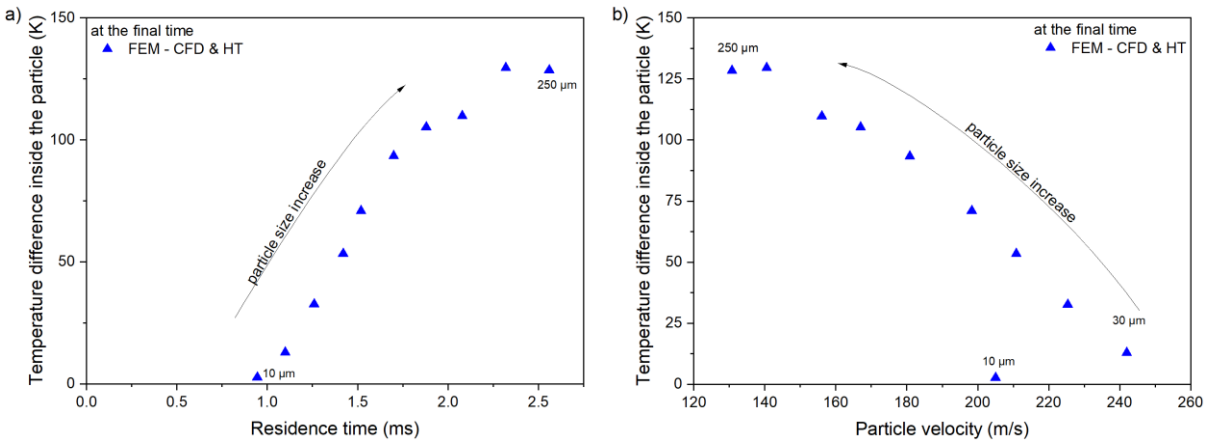

Figure 9: Largest temperature difference inside the particle in function of a) the particle resident time and b) the particle velocity for the different particle sizes.

In Figure 10, the temperature distribution of a 60 µm diameter particle is plotted for different case scenario to investigate the influence of the time dependent gas properties. The particle temperature distribution is similar to the one obtained by Raoelison et al. [11], axisymmetric temperature distribution, consequence of the model definition. However, two main differences compared to that work can be observed. (i) The temperature difference inside the particle is much larger in the case of

polymer particles than for metallic particles (at least 55 K compared to 3 K). (ii) the bottom of the particle is heated through the vortices generated during the particle's flight.

Considering that all gas properties (temperature, relative velocity, and pressure) are time dependent, such as defined in Figure 1, the temperature ranges from 365 K to 420 K (see Figure 10a). Considering a constant gas velocity of 98 m/s corresponding to the average relative velocity of Figure 1, the temperature ranges from 363 K to 434 K (see Figure 10b). On the contrary, when all the gas properties are constant ($\langle V_g \rangle$=98 m/s, T_g=680 K, and P_g=0.4 MPa corresponding to the gas characteristics in the cold spray chamber), the temperature ranges from 410 K to 617 K (see Figure 10c). Thus, the flow field around the particle largely influences the temperature distribution within the particle. The more accurate the gas inlet/outlet conditions, the more precise the temperature distribution. The results for the other particle diameters are provided in Supplementary file 3.

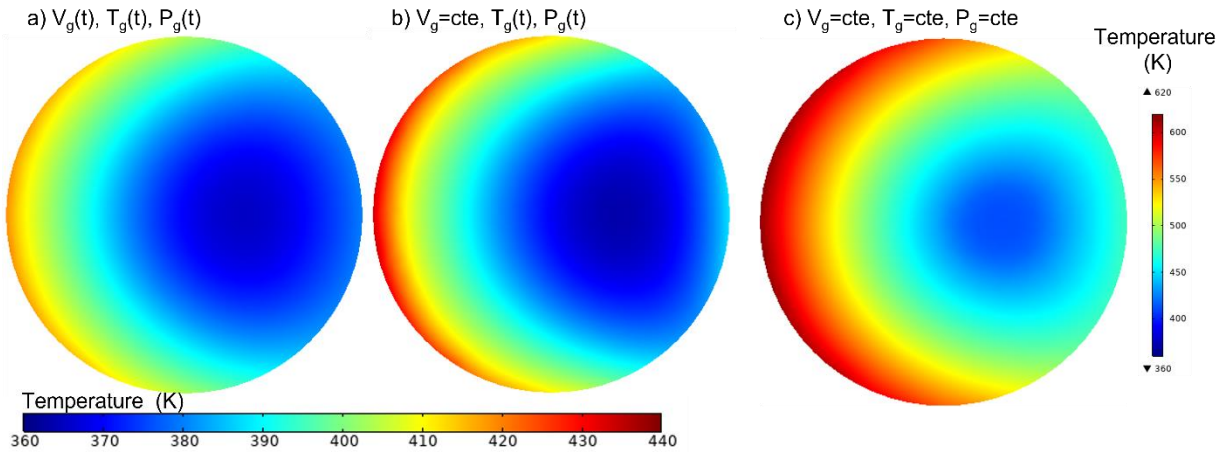

Figure 10: Temperature distribution of a 60 µm particle before impact. a) The gas properties are time dependent such as described in Figure 1. b) The gas temperature and pressure are time dependent, and average constant velocity ($\langle V_g \rangle$=98 m/s) is considered. c) The gas properties are constant. The gas velocity is averaged over the entire flying time ($\langle V_g \rangle$=98 m/s). The gas temperature and pressure are 680 K and 0.4 MPa, respectively, corresponding to the gas characteristics in the cold spray chamber. The temperature distribution is obtained from the particle cross-section. The flow is coming from the left.

3.4. Fluid dynamics around the particle

The evolution of the streamlines around the particle is presented in Figure 11 for a 60 µm diameter particle inside the cold spray nozzle. In the supersonic region (see Figure 11a), asymmetric vortices appear in the bottom of the particle. These vortices will contribute to heating the particle's south pole explaining the presence of a colder area in the particle core. When the flow becomes subsonic, the vortices disappear (see Figure 11b and 11d). However, at the intersection between the two nozzle sections, even though the flow remains subsonic, vortices once again appear in the south pole region of the particle. The reason for such behavior is due to the flow shock and the second particle acceleration inside the nozzle.

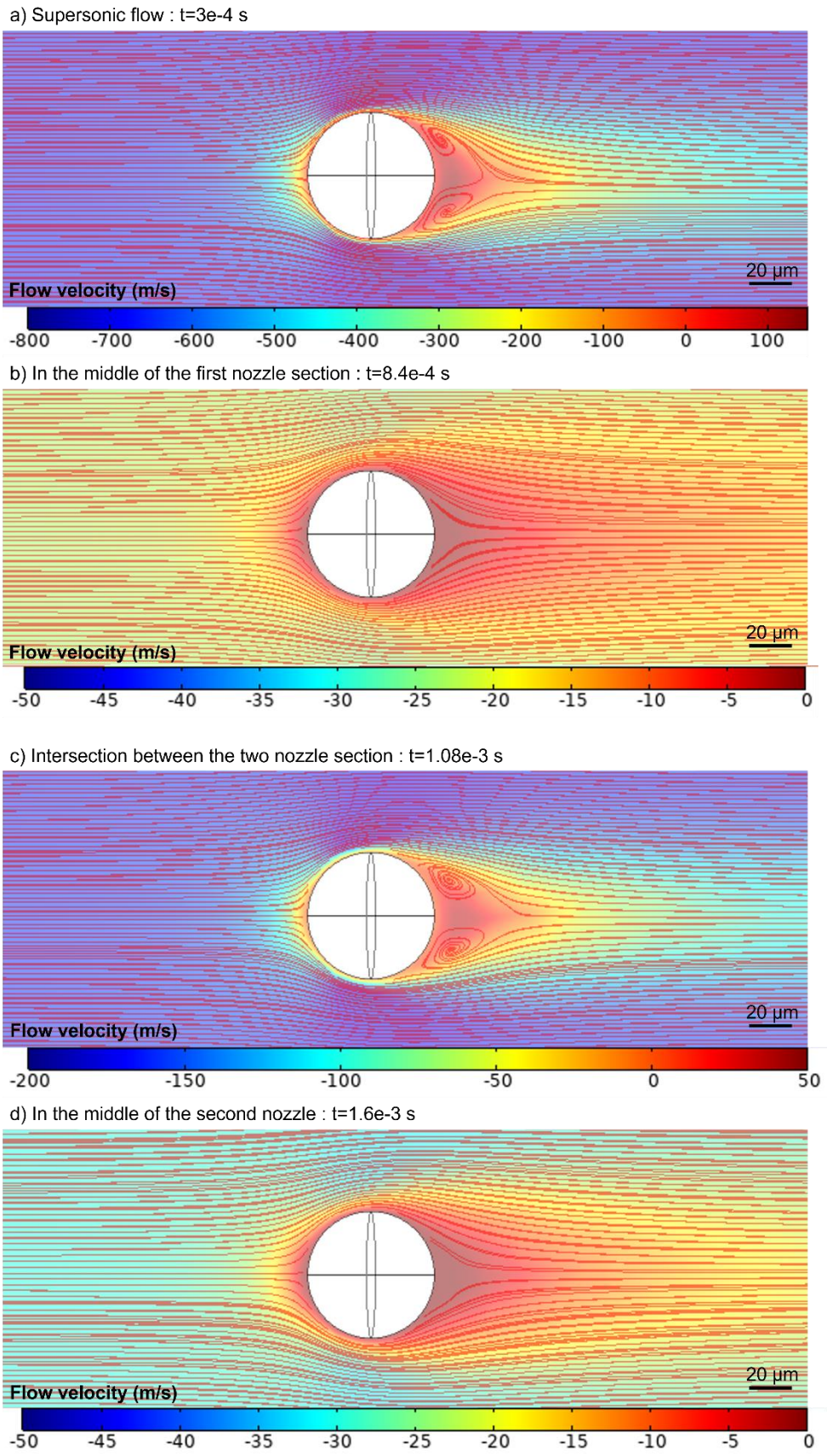

Figure 11: Evolution of the gas flow velocity around a 60 µm diameter particle during its flight. a) in the supersonic region, b) in the middle of the first nozzle, c) at the intersection between the two nozzles (second particle acceleration), d) in the middle of the second nozzle. The flow is coming from the left.

3.5. Influence of the powder feeding rate

During cold spray process, it is usually admitted that particles are well diluted in the flow field. Therefore, the particles should have only a limited effect on the flow field, and all particles should be in a similar state. Here, this assumption will be checked as well as its influence on the flow field.

Assuming that all the feedstock is composed of the same particle size, and considering that the particle feeding rate (FR) equals to 7.5×10^{-5} kg s^{-1} [35], the distance between two particles, d_{2p}, is summarized in Table 3 for different particles diameters. This distance, calculated based on the particle residence time for each particle size, and while assuming uniform particle distribution, is given by:

$$d_{2p} = \left(\frac{V_{nozzle} \times m_p}{FR \times time}\right)^{1/3} \quad (27)$$

where V_{nozzle} is the volume of the nozzle.

Table 3: Distance between two particles for a given diameter. The feeding rate is set at 7.5×10^{-5} *kg* s^{-1} *and the particle residence distance corresponds to the nozzle length (240 mm) (according to the experiments of Ravi et al. [28,35]. The particle residence time is given by the CFD simulations [36] for each particle size. The difference in the particle residence time comes from the difference in the particle velocity directly linked to the particle size.*

Diameter (µm)	**10**	**30**	**45**	**60**	**75**	**100**	**125**	**150**	**200**	**250**
Particle residence time (ms)	1.03	1.30	1.49	**1.70**	1.85	2.12	2.33	2.56	2.89	3.20
Maximum number of particles travelling together inside the nozzle	156954	7337	2492	**1199**	668	323	182	116	55	31
Distance between 2 particles (mm)	0.29	0.80	1.15	**1.47**	1.79	2.28	2.76	3.21	4.11	4.97
Distance between 2 particles (diameters)	29	26.8	25.7	**24.5**	23.9	22.8	22.1	21.4	20.6	19.9

The biggest particles oppose more resistance to the gas flow (increase of the drag force) resulting in low velocities compared to smaller diameters, and, consequently, in the increase of the residence time of the particles, as shown in Table 3. Thus, it takes longer time to travel the same distance if the velocity of the particle decreases. In addition, as the particle diameter is bigger, less particles are needed to achieve the feeding rate leading to less particles travelling at the same time inside the nozzle. Based on the particle size, residence time, the estimation of the number of particles inside the nozzle, and the volume of the nozzle, the distance between two particles inside the nozzle has been estimated. The distance between two particles increases with the diameter (for a given feeding rate). However, reported this distance to the equivalent diameter, this one decreases with the increasing diameter. This point is quite important when analyzing the flow field in the vicinity of the particle. The larger the particle, the greater the disturbance of the flow field with higher probability of overlapping the disturbance caused on the flow field by two successive particles.

In the investigation by Ravi et al. [21], the particle feedstock is reduced to 45~63 µm particles. Thus, for the sake of the discussion, only the influence of the feeding rate on the 60 µm particles will be investigated.

3.5.1. Assumption: d_v=0

Assuming d_v=0 means that the second particle is directly in the wake of the first one. The obstruction of the gas flow hitting directly the second particle is therefore maximal, coupled with the strong influence of the wake induced by the first particle. As observed in Figure 12, when the two particles are close to each other, equivalent to an important feeding rate, the particle thermal gradient is less significant, and the particle average temperature is around 20 K lower than initially observed (see Figure 13). Thus, the interparticle interaction cannot be ignored anymore and will have considerable effect on the gas flow. Therefore, the main assumption of the particles being well diluted in the flow field is not valid anymore when the feeding rate is high, and a new model must be designed to consider the interparticle interactions and the particle influence on the flow field.

When decreasing the feeding rate, the temperature difference within Particle 2 tends towards a plateau equivalent to the one observed for Particle 1. In that case, the particle temperature distribution is very similar between Particle 1 and Particle 2. However, the average particle temperature of Particle 2 remains slightly below Particle 1 temperature (3 to 5 K). This is due to Particle 2 still being affected by the wake of Particle 1.

By investigating the evolution of the particle temperature along the axisymmetric axis for the two particles (see Figure 14), it can be observed that the influence of Particle 2 on Particle 1 is limited even for a high feeding rate. In comparison, the influence of Particle 1 on Particle 2 appears preponderant as the gas temperature in front of Particle 2 decreases with Particle 2 approaching Particle 1.

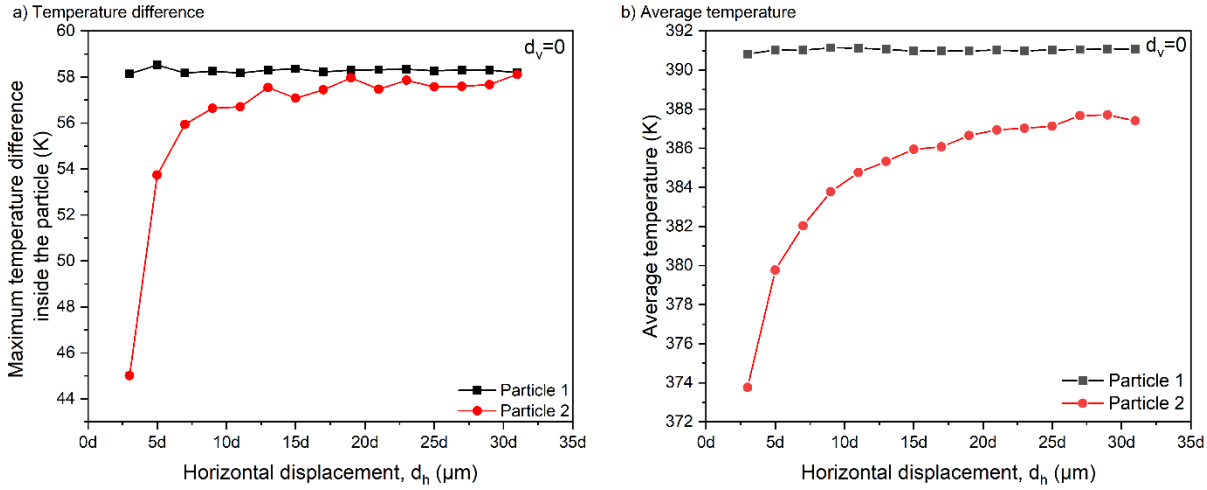

Figure 12: a) Maximum temperature difference (T_{max}- T_{min}) inside the particle and b) average temperature of Particle 1 and Particle 2. The vertical distance is set to 0.

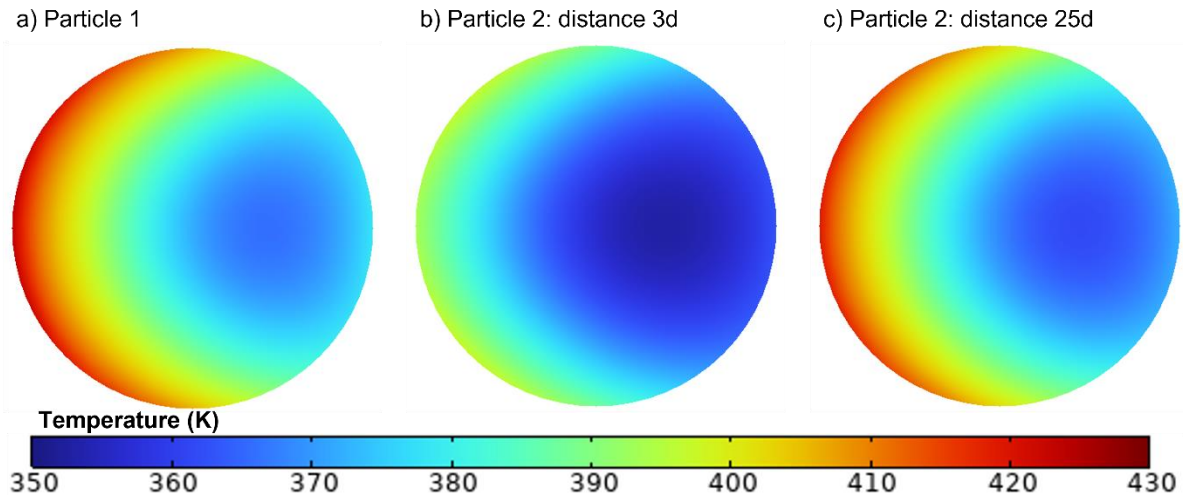

Figure 13: Cross-sectional particle temperature distribution for the a) Particle 1 and Particle 2 located at b) 3d (equivalent feeding rate: 4.1×10^{-2} kg/s) and c) 25d (equivalent feeding rate: 7.1×10^{-5} kg/s) for a 60 µm diameter particle. The flow is coming from the left. The flow is coming from the left.

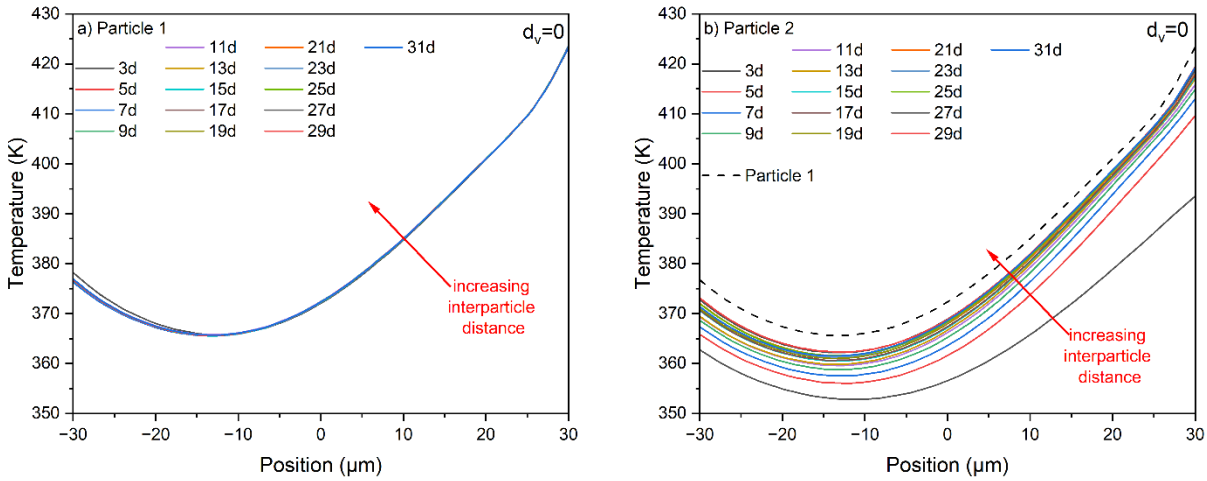

Figure 14: Evolution of the particle temperature along the axisymmetric axis defined in Figure 3.

3.5.2. Assumption: d_h=3d

Particles do not have to be strictly in the wake to each other. When travelling inside the nozzle, each particle follows its own trajectory, independently to each other as the particle flow is assumed to be well diluted in the gas flow. However, as previously shown, this is not the case when d_h=3d, which is the case investigated in this section.

As presented in Figure 15, when Particle 2 is not in the exact axis of Particle 1, the temperature difference within the particle is similar at what it is observed in Particle 1. However, the average temperature is lower because only a part of the heat is provided by the gas flow leading to a non-axisymmetric temperature distribution within the particle, as reported in Figure 16. For the two particles to be considered in the same thermal state, a minimal vertical distance of 1.2d should be observed (see Figure 15b).

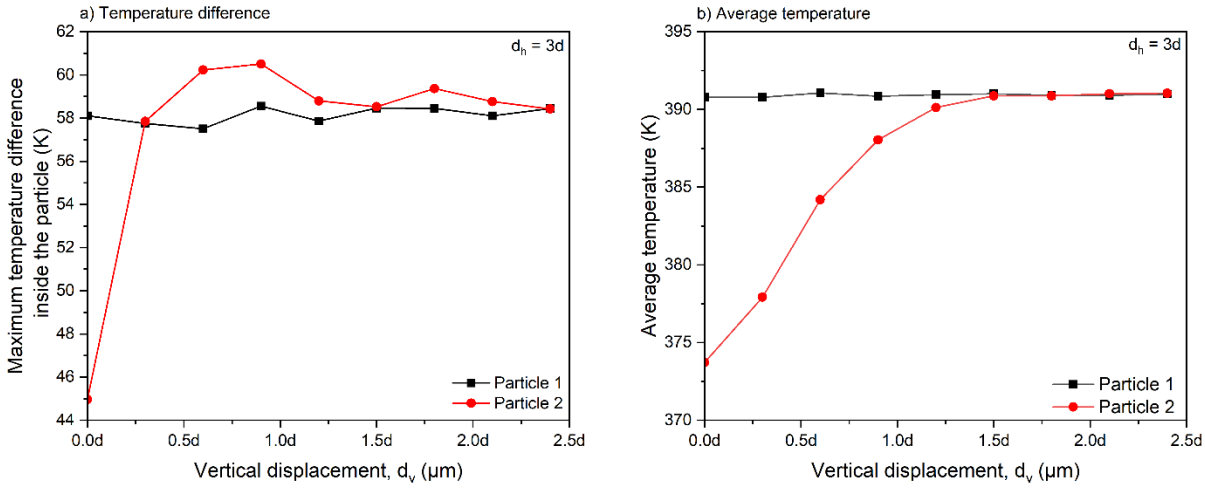

Figure 15: a) Maximum temperature difference (T_{max}- T_{min}) inside the particle and b) average temperature of Particle 1 and Particle 2. The horizontal distance is set to 3d.

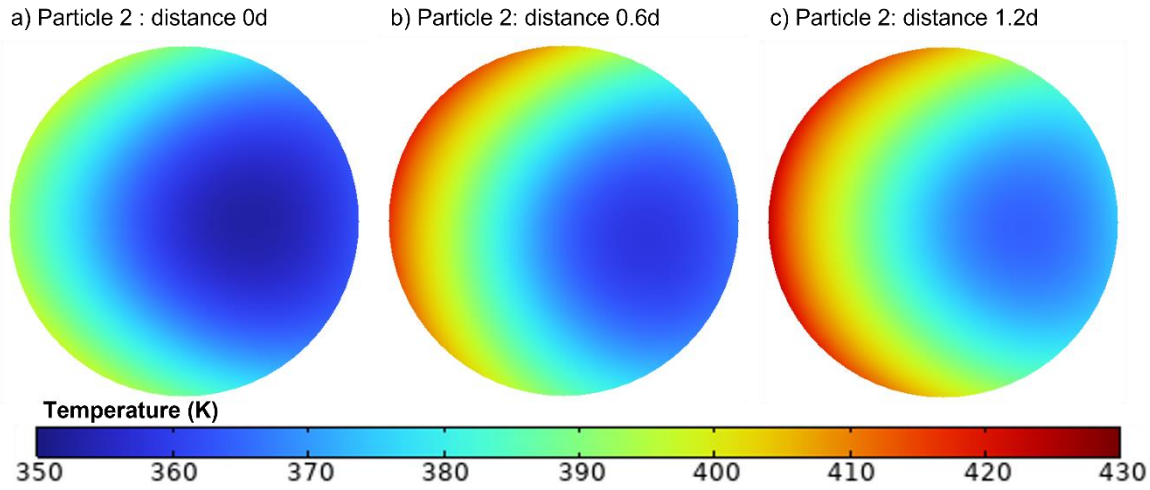

Figure 16: Cross-sectional particle temperature distribution for the and Particle 2 located at a) 0d, b) 0.3d, and c) 1.2d for a 60 µm diameter particle. The equivalent feeding rate is: 4.1×10^{-2} kg/s. The flow is coming from the left.

When looking at the flow streamlines (see Figure 17), it appears evident that the flow is disturbed by the presence of the second particle in the vicinity of the first one. This highly influence the heating of the second particle which does not receive the same amount of energy as the first one. Thus, the two particles influence each other. In that case, one particle in the flow field cannot be considered as an isolated system anymore, and the interparticle influence needs to be considered as well as the evolution of the flow field around.

However, when the vertical distance is large enough (greater than 1.2d), and the flow field behind the particle is not disturbed by the presence of the second particle, one particle in the flow field can be considered as an isolated system.

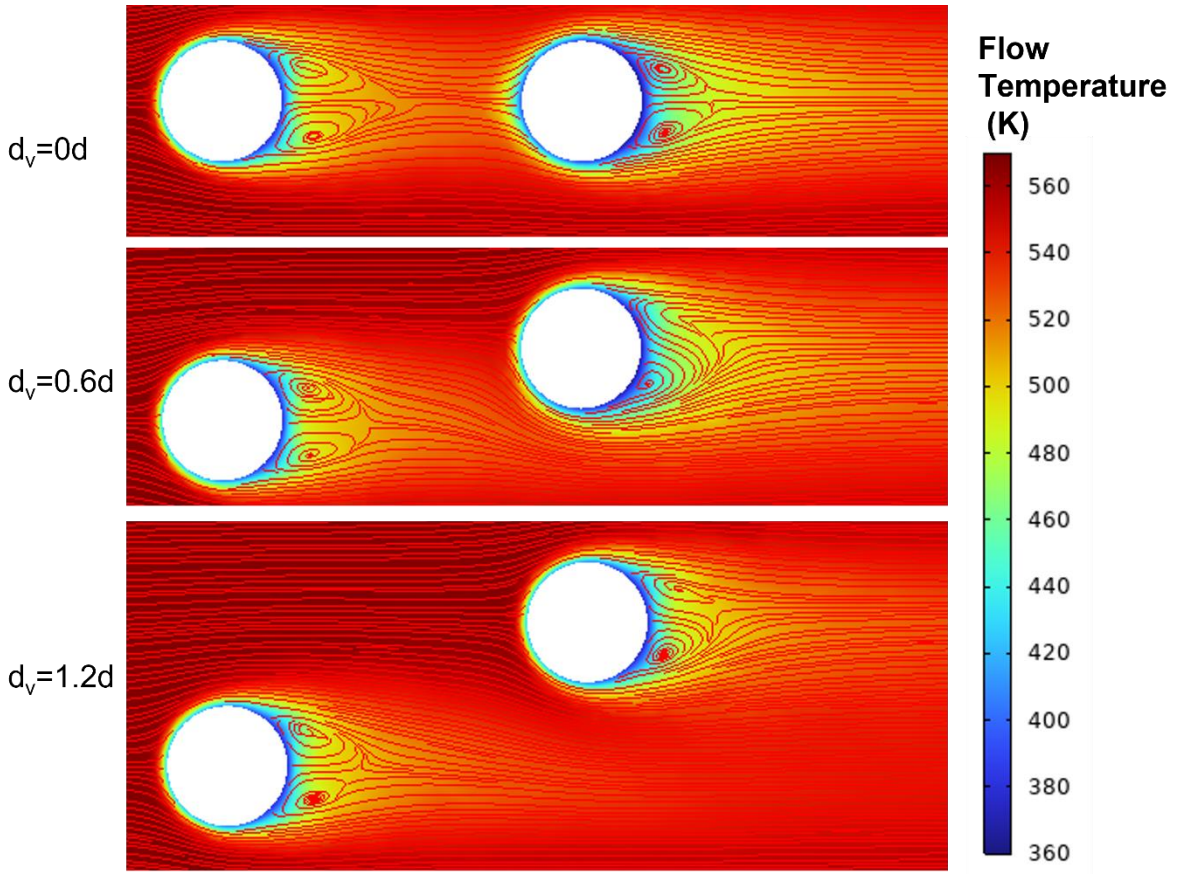

Figure 17: Evolution of the flow temperature and flow field (streamlines) around the particles at the final time for different values of d_v. d_h is set at 3d. The flow is coming from the left.

3.5.3. Assumption: d_h=24.5d

According to the particle feeding rate used by Ravi et al. [35] in their experiments, the distance between two particles should be equivalent to 24.5d. Thus, at this distance, the temperature difference inside the particle (see Figure 18a) is equivalent between Particle 1 and Particle 2, whatever the vertical position of Particle 2. However, when looking at the average temperature inside the particle (see Figure 18b), the particle temperature continues to increase when Particle 2 drives out from the wake of Particle 1. Thus, even at a distance of 24d, the first particle slightly influences the second particle.

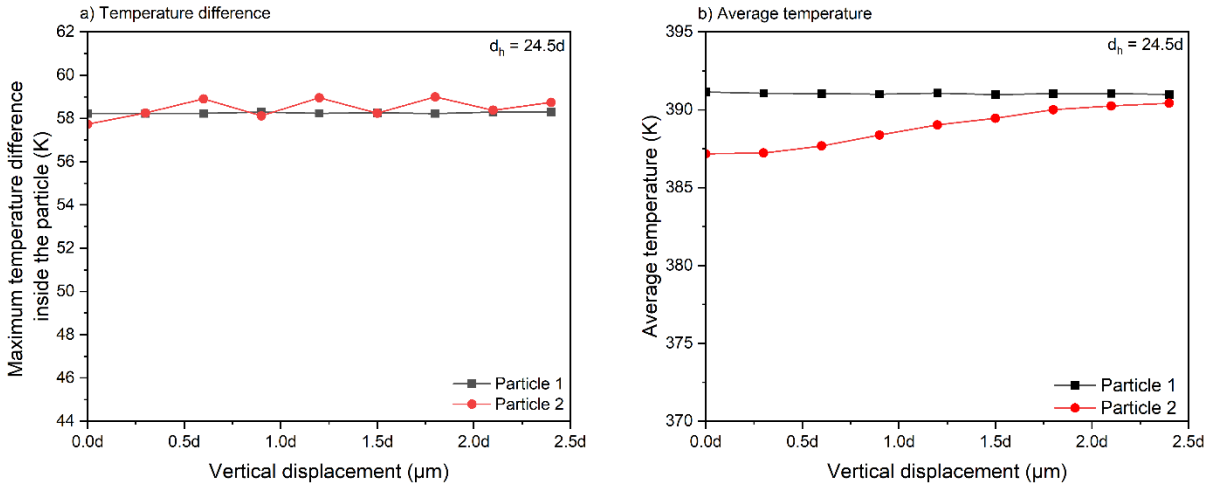

Figure 18: a) Maximum temperature difference (T_{max}- T_{min}) inside the particle and b) average temperature of Particle 1 and Particle 2. The horizontal distance is set to 24.5d.

Based on this observation, it is unlikely that the particle temperature exhibits an axisymmetric distribution when Particle 2 is in the wake of Particle 1. However, at 2.4d, Particle 2 exhibits the same temperature distribution as Particle 1 (see Figure 19).

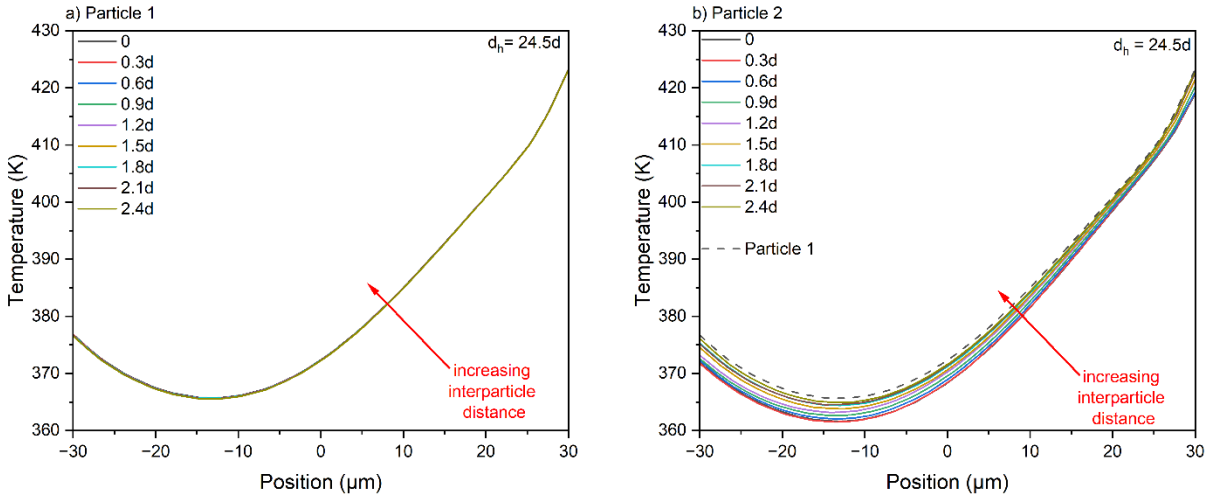

Figure 19: Evolution of the particle temperature along the axisymmetric axis defined in Figure 3. The horizontal distance is set at 24.5d.

On Figure 20, the axisymmetry of the particle temperature distribution does not appear as identifiable as it is on Figure 16. However, according to Figure 18b and Figure 19, a small drift exists even though it is limited to 3-4 K when d_v is lower than 2.4d.

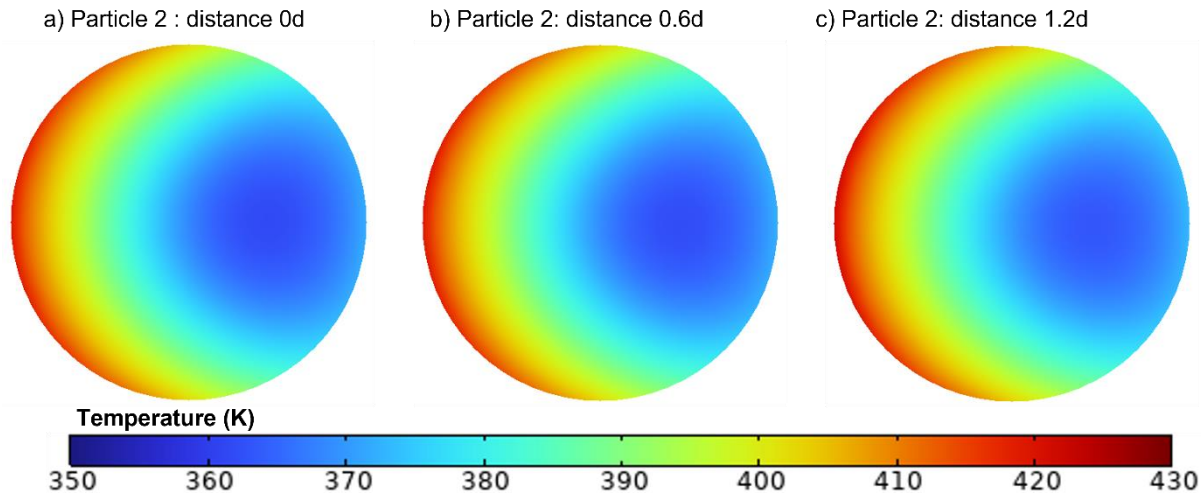

Figure 20: Cross-sectional particle temperature distribution for the and Particle 2 located at a) 0d, b) 0.3d, and c) 1.2d for a 60 µm diameter particle. The equivalent feeding rate is: 7.5×10^{-5} kg/s. The flow is coming from the left.

4. Conclusion

This paper investigates the evolution of the polymer particle temperature during the cold spray process. The operating conditions and the nozzle geometry in this study are taken from the experiments of Ravi et al. [21] with UHMWPE particles sprayed at 0.4 MPa and 680 K. The obtained findings from this study can be transposed to other polymers.

The present paper highlights and proves the existence of a thermal gradient within the polymer particles. This aspect is of importance when considering the temperature and strain rate sensitivity of polymer material. Thus, even before the impact on the substrate, the particle exhibits a thermal gradient, and therefore, a gradient of mechanical properties that must be considered when modelling the particle impact. The temperature distribution inside the particle is decided by the flow field developed around the particle during its flight.

When several particles fly next to each other inside the nozzle, the feeding rate plays an important role of the interparticle interaction. If the particle feeding rate is too high, the particles are not diluted in the nozzle anymore, and particles influence the flow field as well as their neighbors. However, when the feeding rate is low and the particles are well diluted in the nozzle, the particle interaction is reduced, and only a temperature difference of 3-4 K maximum is observed between two particles.

Finally, understanding polymer coating by cold spray process starts with a complete understanding of the particle history during their flight. Obtaining this information will help in the modelling of the particle impact. However, it is important to note that in the case of polymer particles, strong assumptions have been made, such as spherical particles. Unlike metallic powder, polymer particles exhibit a coarse geometry. The probability of particle rotation inside the nozzle is not excluded, but it is limited as the particle shape leads to their orientation in the direction which minimize their drag. Nevertheless, this study gives good insight into non-measurable phenomena and transient heating of polymer particles during their flight.

Acknowledgments

The authors would like to acknowledge the Institute of Fluid Science at Tohoku University, which supported this research through the grants J21Ly08 and J22Ly09 under the label of the LyC Collaborative Research Project.

Conflict of interests

The authors declare that they have no conflict of interest.

References

[1] A.P. Alkhimov, V. Kosarev, N. Nesterovich, A. Papyrin, M. Shushpanov, Device for applying coatings, 1618777, 1990.

[2] A.P. Alkhimov, A.N. Papyrin, V.F. Kosarev, N.I. Nesterovich, M.M. Shushpanov, Gas-dynamic spraying method for applying a coating, US Patent. (1994).

[3] K. Ravi, W.L. Sulen, C. Bernard, Y. Ichikawa, K. Ogawa, Fabrication of micro-/nano-structured super-hydrophobic fluorinated polymer coatings by cold-spray, Surface and Coatings Technology. 373 (2019) 17–24. https://doi.org/10.1016/j.surfcoat.2019.05.078.

[4] E.B. Caldona, D.W. Smith, D.O. Wipf, Protective action of semi-fluorinated perfluorocyclobutyl polymer coatings against corrosion of mild steel, Journal of Materials Science. 55 (2020) 1796–1812.

[5] T. Schmidt, F. Gärtner, H. Assadi, H. Kreye, Development of a generalized parameter window for cold spray deposition, Acta Materialia. 54 (2006) 729–742.

[6] M. Hassani-Gangaraj, D. Veysset, K.A. Nelson, C.A. Schuh, In-situ observations of single micro-particle impact bonding, Scripta Materialia. 145 (2018) 9–13. https://doi.org/10.1016/j.scriptamat.2017.09.042.

[7] A. Nastic, B. Jodoin, Evaluation of Heat Transfer Transport Coefficient for Cold Spray Through Computational Fluid Dynamics and Particle In-Flight Temperature Measurement Using a High-Speed IR Camera, Journal of Thermal Spray Technology. 27 (2018) 1491–1517. https://doi.org/10.1007/s11666-018-0787-y.

[8] J. Fiebig, J.-P. Gagnon, G. Mauer, E. Bakan, R. Vaßen, In-Flight Measurements of Particle Temperature and Velocity with a High-Speed IR Camera During Cold Gas Spraying of In718 and TiAlCrNb, Journal of Thermal Spray Technology. 31 (2022) 2013–2024. https://doi.org/10.1007/s11666-022-01426-9.

[9] M. Alletto, M. Breuer, One-way, two-way and four-way coupled LES predictions of a particle-laden turbulent flow at high mass loading downstream of a confined bluff body, International Journal of Multiphase Flow. 45 (2012) 70–90. https://doi.org/10.1016/j.ijmultiphaseflow.2012.05.005.

[10] H. Katanoda, Numerical Simulation of Temperature Uniformity within Solid Particles in Cold Spray, Journal of Solid Mechanics and Materials Engineering. 2 (2008) 58–69. https://doi.org/10.1299/jmmp.2.58.

[11] R.N. Raoelison, M.R. Guéchi, E. Padayodi, In-flight temperature of solid micrometric powders during cold spray additive manufacturing, International Journal of Thermal Sciences. 157 (2020) 106422. https://doi.org/10.1016/j.ijthermalsci.2020.106422.

[12] C. Bernard, N. Bahlouli, C. Wagner-Kocher, J. Lin, S. Ahzi, Y. Rémond, Multiscale description and prediction of the thermomechanical behavior of multilayered plasticized PVC under a wide range of strain rate, Journal of Materials Science. 53 (2018) 14834–14849.

[13] T. Deplancke, O. Lame, F. Rousset, R. Seguela, G. Vigier, Mechanisms of chain reentanglement during the sintering of UHMWPE nascent powder: effect of molecular weight, Macromolecules. 48 (2015) 5328–5338. https://doi.org/10.1021/acs.macromol.5b00618.

[14] S. Humbert, O. Lame, G. Vigier, Polyethylene yielding behaviour: What is behind the correlation between yield stress and crystallinity?, Polymer. 50 (2009) 3755–3761. https://doi.org/10.1016/j.polymer.2009.05.017.

[15] J. Richeton, S. Ahzi, K. Vecchio, F. Jiang, R. Adharapurapu, Influence of temperature and strain rate on the mechanical behavior of three amorphous polymers: characterization and modeling of the compressive yield stress, International Journal of Solids and Structures. 43 (2006) 2318–2335.

[16] C. Bernard, H. Takana, G. Diguet, K. Ravi, O. Lame, K. Ogawa, J.-Y. Cavaillé, Thermal gradient of in-flight polymer particles during cold spraying, Journal of Materials Processing Technology. 286 (2020) 116805.
[17] T.W. Bacha, N.K. Singh, I.M. Nault, B. Koohbor, F.M. Haas, J.F. Stanzione, Thermal Gradients Govern Impact Dynamics in Thermoplastic Polymer Cold Spray, Journal of Thermal Spray Technology. 30 (2021) 2034–2049.
[18] T. Deplancke, O. Lame, F. Rousset, I. Aguili, R. Séguéla, G. Vigier, Diffusion versus cocrystallization of very long polymer chains at interfaces: experimental study of sintering of UHMWPE nascent powder, Macromolecules. 47 (2014) 197–207.
[19] C.A. Bernard, H. Takana, O. Lame, K. Ogawa, J.-Y. Cavaillé, Influence of the Nozzle Inner Geometry on the Particle History During Cold Spray Process, Journal of Thermal Spray Technology. (2022). https://doi.org/10.1007/s11666-022-01407-y.
[20] ANSYS, Inc., Ansys fluent tutorial guide, ANSYS, Inc., Canonsburg, PA, USA, 2017.
[21] K. Ravi, Y. Ichikawa, T. Deplancke, K. Ogawa, O. Lame, J.-Y. Cavaille, Development of ultra-high molecular weight polyethylene (UHMWPE) coating by cold spray technique, Journal of Thermal Spray Technology. 24 (2015) 1015–1025. https://doi.org/10.1007/s11666-015-0276-5.
[22] K. Ravi, Y. Ichikawa, K. Ogawa, T. Deplancke, O. Lame, J.-Y. Cavaille, Mechanistic study and characterization of cold-sprayed ultra-high molecular weight polyethylene-nano-ceramic composite coating, Journal of Thermal Spray Technology. 25 (2016) 160–169. https://doi.org/10.1007/s11666-015-0332-1.
[23] J. Bicerano, Prediction of polymer properties, CRC Press, 2002.
[24] D.W. Van Krevelen, K. Te Nijenhuis, Properties of polymers: their correlation with chemical structure; their numerical estimation and prediction from additive group contributions, Elsevier, 2009.
[25] T. Schmidt, H. Assadi, F. Gärtner, H. Richter, T. Stoltenhoff, H. Kreye, T. Klassen, From Particle Acceleration to Impact and Bonding in Cold Spraying, Journal of Thermal Spray Technology. 18 (2009) 794–808. https://doi.org/10.1007/s11666-009-9357-7.
[26] H. Assadi, T. Schmidt, H. Richter, J.-O. Kliemann, K. Binder, F. Gärtner, T. Klassen, H. Kreye, On Parameter Selection in Cold Spraying, Journal of Thermal Spray Technology. 20 (2011) 1161–1176. https://doi.org/10.1007/s11666-011-9662-9.
[27] M. Winnicki, A. Małachowska, G. Dudzik, M. Rutkowska-Gorczyca, M. Marciniak, K. Abramski, A. Ambroziak, L. Pawłowski, Numerical and experimental analysis of copper particles velocity in low-pressure cold spraying process, Surface and Coatings Technology. 268 (2015) 230–240. https://doi.org/10.1016/j.surfcoat.2014.11.059.
[28] K. Ravi, T. Deplancke, K. Ogawa, J.-Y. Cavaillé, O. Lame, Understanding deposition mechanism in cold sprayed ultra high molecular weight polyethylene coatings on metals by isolated particle deposition method, Additive Manufacturing. 21 (2018) 191–200.
[29] N.K. Singh, K.Z. Uddin, J. Muthulingam, R. Jha, B. Koohbor, Analyzing the Effects of Particle Diameter in Cold Spraying of Thermoplastic Polymers, Journal of Thermal Spray Technology. 30 (2021) 1226–1238. https://doi.org/10.1007/s11666-021-01219-6.
[30] H. Koivuluoto, A Review of Thermally Sprayed Polymer Coatings, Journal of Thermal Spray Technology. (2022). https://doi.org/10.1007/s11666-022-01404-1.
[31] W.E. Ranz, J.R. Marshall, Evaporation from drops - Part I, Chem. Eng. Prog. 48 (1952) 141–146.
[32] C. Borgnakke, R.E. Sonntag, Fundamentals of Thermodynamics, SI version, Eighth Edition, John Wiley & Sons, 2014.
[33] W. Sutherland, The viscosity of mixed gases, The London, Edimburgh, and Dunlin Philosophical Magazine and Journal of Science. 40 (1895) 421–431.
[34] J. Hilsenrath, C. Beckett, W. Benedict, L. Fano, H. Hoge, J. Masi, R. Nuttall, Y. Touloukian, Tables of Thermodynamic and Transport Properties of Air, Argon, Carbon Dioxide, Carbon Monoxide, Hydrogen, Nitrogen, Oxygen, and Steam, Pergamon Press, 1960.

[35] K. Ravi, Mechanistic understanding of high strain rate impact behavior of ultra-high molecular weight polyethylene and the mechanism of coating formation during cold spraying, PhD Thesis, Tohoku University and INSA Lyon, 2018.
[36] C.A. Bernard, H. Takana, O. Lame, K. Ogawa, J.-Y. Cavaillé, Influence of the Nozzle Inner Geometry on the Particle History During Cold Spray Process, Journal of Thermal Spray Technology. 31 (2022) 1776–1791. https://doi.org/10.1007/s11666-022-01407-y.